Research article

Qingqing Cheng*, Juncheng Wang, Ling Ma, Zhixiong Shen, Jing Zhang, Xiaoying Zheng, Tao Chen, Ye Yu, Dong Yu, Qiong He, Wei Hu, Tao Li*, Songlin Zhuang and Lei Zhou*

Achromatic terahertz Airy beam generation with dielectric metasurfaces

https://doi.org/10.1515/nanoph-2020-0536
Received September 22, 2020; accepted November 29, 2020; published online December 14, 2020

Abstract: Airy beams exhibit intriguing properties such as nonspreading, self-bending, and self-healing and have attracted considerable recent interest because of their many potential applications in photonics, such as to beam focusing, light-sheet microscopy, and biomedical imaging. However, previous approaches to generate Airy beams using photonic structures have suffered from severe chromatic problems arising from strong frequency dispersion of the scatterers. Here, we design and fabricate a metasurface composed of silicon posts for the frequency range 0.4–0.8 THz in transmission mode, and we experimentally demonstrate achromatic Airy beams exhibiting autofocusing properties. We further show numerically that a generated achromatic Airy-beam-based metalens exhibits self-healing properties that are immune to scattering by particles and that it also possesses a larger depth of focus than a traditional metalens. Our results pave the way to the realization of flat photonic devices for applications to noninvasive biomedical imaging and light-sheet microscopy, and we provide a numerical demonstration of a device protocol.

Keywords: achromatism; Airy beam; metasurface; Pancharatnam–Berry phase; transmission phase.

***Corresponding authors: Qingqing Cheng**, School of Optical-Electrical and Computer Engineering, University of Shanghai for Science and Technology, Shanghai 200093, China; **Tao Li**, National Laboratory of Solid State Microstructures, College of Engineering and Applied Sciences, Nanjing University, Nanjing 210093, China; and **Lei Zhou**, State Key Laboratory of Surface Physics, Key Laboratory of Micro and Nano Photonic Structures (Ministry of Education), Department of Physics, Fudan University, Shanghai 200438, China, E-mail: qqcheng@usst.edu.cn (Q. Cheng), taoli@nju.edu.cn (T. Li), phzhou@fudan.edu.cn (L. Zhou). https://orcid.org/0000-0001-7386-6081 (Q. Cheng)
Juncheng Wang, Ling Ma, Jing Zhang, Tao Chen, Ye Yu, Dong Yu and Songlin Zhuang, School of Optical-Electrical and Computer Engineering, University of Shanghai for Science and Technology, Shanghai 200093, China, E-mail: 871272051@qq.com (J. Wang), malingouc@163.com (L. Ma), 1012826389@qq.com (J. Zhang), 573153525@qq.com (T. Chen), 928979399@qq.com (Y. Yu), 893155049@qq.com (D. Yu), slzhuangx@aliyun.com (S. Zhuang)
Zhixiong Shen and Wei Hu, Key Laboratory of Intelligent Optical Sensing and Manipulation and College of Engineering and Applied Sciences, Nanjing University, Nanjing 210093, China, E-mail: njuzxshen@163.com (Z. Shen), huwei@nju.edu.cn (W. Hu)
Xiaoying Zheng and Qiong He, State Key Laboratory of Surface Physics, Key Laboratory of Micro and Nano Photonic Structures (Ministry of Education), Department of Physics, Fudan University, Shanghai 200438, China, E-mail: 18110190014@fudan.edu.cn (X. Zheng), qionghe@fudan.edu.cn (Q. He). https://orcid.org/0000-0002-4966-0873 (Q. He)

1 Introduction

As a nontrivial solution of the paraxial equation of light [1], an Airy beam exhibits many remarkable features, such as self-bending (even in the absence of any external potential field), nonspreading, and self-healing after diffractions by obstacles [2–7]. Owing to these attractive properties, Airy beams have many potential applications in photonics, such as for particle manipulation [8], as light bullets [9, 10], for super-resolution imaging [11, 12], as autofocusing Airy (AFA) beams [13–15], and for light-sheet microscopy [16]. In 2007, Siviloglou and Christodoulides [17] proposed a truncated form of Airy beam and then realized it experimentally. Such a simplified version of an Airy beam, possessing finite energy, preserves all the key features of an ideal Airy beam and has therefore attracted much attention recently.

The conventional generation of Airy beams utilizes spatial light modulators (SLMs), which are bulky and lack fine spatial resolution [18–20]. The Airy beams generated in this way do not exhibit good qualities, and the bulky generation systems are unsuitable for practical applications. Recently, plasmonic Airy beams [19, 21, 22] have been successfully generated on metallic surfaces on which are placed nanoscatterers that have been carefully designed to convert impinging light to surface plasmon waves with the desired amplitudes and phases. Although these devices are compact and exhibit improved spatial resolution, the

Open Access. © 2020 Qingqing Cheng et al., published by De Gruyter. This work is licensed under the Creative Commons Attribution 4.0 International License.

generated Airy beams can flow only on certain planes, and the working efficiencies are quite low owing to the intrinsic losses and nonideal performances of the metallic nanoscatterers that are used. For practical applications, it is highly desirable to have ultracompact and broadband devices that can efficiently generate Airy beams in free space.

Metasurfaces, ultrathin metamaterials consisting of subwavelength microstructures (e.g., meta-atoms) with tailored optical properties, offer a fascinating platform on which to realize planar photonic devices with desired functionalities [23–37]. In the past few years, Airy beams have been successfully generated by carefully designed metadevices constructed from meta-atoms of different types (metallic or dielectric resonators) that can scatter electromagnetic waves with desired amplitudes and phases [20,38–40]. These ultrathin devices can generate Airy beams in free space with relatively high efficiencies. However, since the phase responses of the adopted resonating meta-atoms typically exhibit Lorentz-like frequency dispersion, such metadevices can usually work only at a specific single frequency at which the system precisely exhibits the phase/amplitude distributions required by the analytical formula. Despite several attempts (using, for example, geometric-phase metasurfaces [38, 39, 41, 42] or double-stacked metasurfaces [40]), the constructed metadevices still suffer from chromatic issues [3,43–48], which hinders their practical application.

In this paper, we experimentally realize achromatic Airy beams in the terahertz (THz) regime with a carefully designed dielectric metasurface. Our metadevice consists of a set of silicon posts with different sizes and orientation angles determined by the requirement to generate the desired phase profile for achromatic Airy beams within a broad frequency band of 0.4–0.8 THz. We demonstrate that the generated achromatic Airy beams exhibit self-healing properties. In addition, an Airy-beam-based metalens is constructed by combining two such achromatic Airy beams and possesses a large depth of focus and robustness against scatterers. Our results stimulate us to propose a device protocol for Airy-beam-based metalens microscopy based on the proposed metasurface.

2 Results and discussions

2.1 Design principle for generation of THz achromatic Airy beams

Rather than using a fixed spatial wavefront to generate a chromatic Airy beam, here we exploit a wavelength-dependent spatial phase based on a silicon metasurface to generate an achromatic Airy beam with the same trajectory. A schematic of the achromatic Airy beam generator is shown in Figure 1(a). The incident THz wave impinges vertically on the metasurface device and the transmitted THz wave follows the trajectory along the white dash line $f(z)$. To realize the achromatic Airy beam, here we study the truncated Airy beam to acquire the wavelength-dependent spatial phase of the achromatic Airy beam. The Airy beam is generated by an initial field distribution in the metasurface plane at $z = 0$, given by $\psi(x, z = 0) = Ai(x)$. Here, we employ the semiclassical approximation to analyze the Airy function. The standard asymptotic forms show that $\psi(x, z = 0)$ is exponentially small for $x > 0$, and hence negligible, and is oscillatory for $x < 0$, the precise expression being

$$\psi(x, z=0) \approx (-\pi^2 x)^{-1/4} \sin\left[\tfrac{2}{3}(-x)^{3/2} + \tfrac{\pi}{4}\right] = A_+ e^{ik\phi_+} + A_- e^{ik\phi_-}),$$

where $\phi_\pm = \mp\frac{2}{3}(-x)^{3/2} + \pi/4$ and $A_\pm = \pm(i/2)(-\pi^2 x)^{-1/4}$ are the initial phases and amplitude functions. The initial phases ϕ_+ and ϕ_- give rise to rays that propagate along the $+x$ and opposite $-x$ directions. Specifically, the ray species ϕ_+ emerges sideways, converging to a caustic along the trajectory $f(z) = (az^2)/4$, where the variable a is equal to $1/(k^2 x_0^3)$, and k and x_0 are the wavenumber and an arbitrary transverse scale. The details of the parabolic trajectory are derived in Note S1 in the Supplementary material. The geometric construction deriving the phase profile is illustrated in Figure 1(b). The parabolic trajectory is indicated by the black dash curve $f(z)$ as shown, and we obtain the corresponding spatial phase function $\varphi(x)$ at the metasurface plane with $z = 0$ that will generate the curve as a caustic. The caustic is constructed as the envelope to a family of rays ϕ_+ such that each point x at the plane $z = 0$ can be functionally related to a point on the caustic via a tangent of slope θ, where $\tan\theta = f'(z) = \mathrm{d}f(z)/\mathrm{d}z$. Since the tangent can be parameterized in terms of x using $f'(z) = [f(z) - x]/z$, we can determine the desired phase distributions by integrating the phase derivative condition:

$$\frac{\mathrm{d}\varphi(x)}{\mathrm{d}x} = k\sin\theta = \frac{kf'(z)}{\sqrt{1 + [f'(z)]^2}}. \tag{1}$$

When the analysis in the preceding discussion is simplified in the paraxial approximation, we obtain the following wavelength-dependent phase profile:

$$\varphi(x, f) = -\frac{4}{3}a^{1/2}\pi(-x)^{3/2} \cdot \frac{f}{c} + \varphi_{\mathrm{shift}}(f) \tag{2}$$

where the value of $\varphi_{\mathrm{shift}}(f)$ represents an integration constant at the frequence of f. To realize an achromatic Airy beam within $f \in [f_{\min} = 0.4\,\mathrm{THz}, f_{\max} = 0.8\,\mathrm{THz}]$ in Figure 1(c),

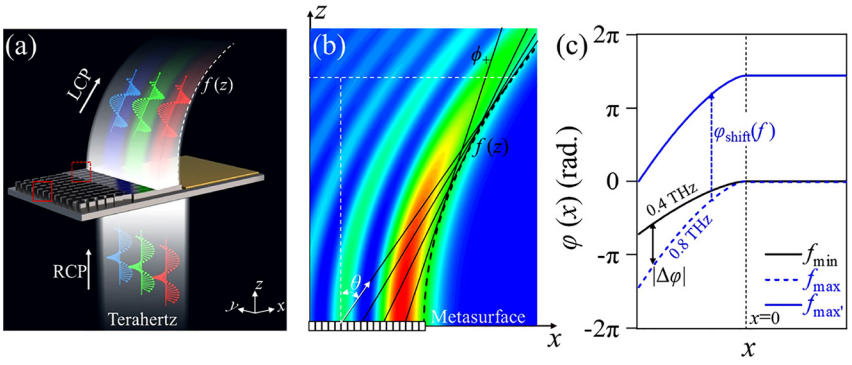

Figure 1: Schematic and phase profile of an achromatic Airy beam.
(a) Schematic of the experimental generation of terahertz (THz) achromatic Airy beams by a silicon metasurface. The transmitted left circular polarization (LCP) THz intensities in the x–z plane fit the parabolic trajectory $f(z)$ for the right circular polarization (RCP) incident light. (b) To determine the phase distribution $\varphi(x,f)$ of the metasurface under design, we draw an auxiliary line (black solid line) tangent to the parabolic asymptotical trajectory $f(z)$ of the desired Airy beam (black dash line) at an arbitrary point, which intersects with x axis exhibiting an angle θ. With $\theta(x)$ function obtained by repeating such a process, we then obtain $\varphi(x,f)$ based on Eq. (1). (c) Phase profile of an achromatic Airy beam within the frequency range $f \in [f_{\min}, f_{\max}]$, where $f_{\min} = 0.4$ THz, $f_{\max} = 0.8$ THz, $\varphi_{\text{shift}} = 820^\circ$ at 0.8 THz, and the arbitrary transverse scale $x_0 = 650$ μm in our design.

we need to design a metasurface exhibiting the phase profile $\varphi(x,f)$, as shown in Eq. 2, for every frequency within the band $[f_{\min}, f_{\max}]$.

We now illustrate how to design such a metasurface exhibiting the desired phase profile. With $\varphi_{\text{shift}}(f)$ term dropped for the moment, we decompose the remaining part of phase profile $\varphi(x,f)$ into two parts, namely a basic phase profile $\varphi_1(x,f)$ representing the phase profile required by the device at $f_{\min}$ and $\varphi_2(x,f)$ the phase difference at other frequencies. Straightforward calculations yield that:

$$\varphi_1(x,f) = -\frac{4\pi a^{1/2}}{3c} x^{3/2} \cdot f_{\min}, \tag{3}$$

and

$$\varphi_2(x,f) = -\frac{4\pi a^{1/2}}{3c} x^{3/2} \cdot (f - f_{\min}). \tag{4}$$

Now our task is to design a series of meta-atoms, which not only yield the required phases required by Eq. (3) at the frequency $f_{\min}$, but also exhibit the different frequency dispersions as dictated by Eq. (4). However, $\varphi_2(x,f)$ exhibits negative slopes against frequency at every point x, which can *not* be realized by any resonating structures exhibiting normal frequency dispersions (i.e., transmission phases are increasing functions of frequency). Fortunately, there is an additional term $\varphi_{\text{shift}}(f)$ in Eq. (2), which can be freely chosen to solve this issue. Specifically, set $\varphi_{\text{shift}}(f) = \alpha \cdot (f - f_{\min})$, we find that:

$$\begin{aligned}\varphi(x,f) &= \varphi_1 + \varphi_2 + \varphi_{\text{shift}} \\ &= -\frac{4\pi a^{1/2}}{3c} x^{3/2} \cdot f_{\min} + \left[-\frac{4\pi a^{1/2}}{3c} x^{3/2} \right. \\ &\quad \left. + \alpha \right] (f - f_{\min}).\end{aligned} \tag{5}$$

Choosing an appropriate α value, we can make the term $\left[-\frac{4\pi a^{1/2}}{3c} x^{3/2} + \alpha \right]$ taking positive values at every position x, so that such frequency-dependent phase profiles can be realizable using resonating meta-atoms.

We proceed to search a series of meta-atoms exhibiting the desired phases (Eq. (3)) at frequency $f_{\min}$ and frequency-variation slopes as required by Eq. (5). The building structures of the silicon metasurface are presented in Figure 2(a) and (b), consisting of solid and inverse rectangular structures on a silicon substrate. To fulfill the complex requirements on the phase responses, we design the metastructures based on a combination of two mechanisms, namely, the resonance mechanism yielding a frequency-dependent transmission phase and the Pancharatnam-Berry (PB) one yielding a frequency-independent phase. Since the PB mechanism is adopted, we assume the incident THz wave to exhibit RCP, and employ finite-difference time-domain (FDTD) simulations to determine the width w and length l of our meta-structures (with fixed lattice period p and etching depth t) based on two criterions: 1) transmission phases exhibit

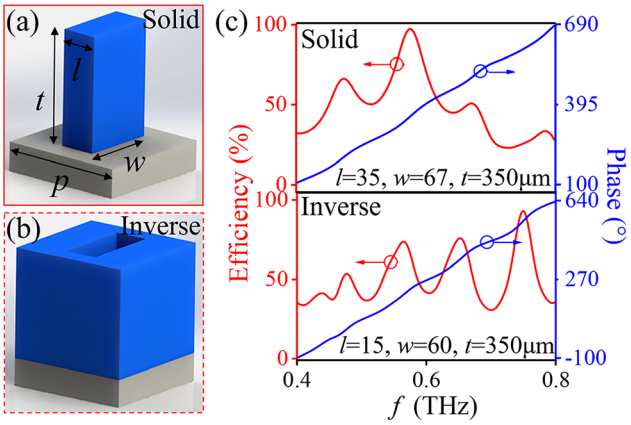

Figure 2: Phase distributions and conversion efficiencies of the solid and inverse structure.
Side views of (a) a solid and (b) an inverse silicon structures with length *l*, width *w*, etching depth *t*, and lattice constant *p* on a silicon substrate. (c) Simulated phase responses (blue curves) and RCP-to-LCP polarization conversion efficiencies (red curves).

linear dependences on frequency with desired slopes; and 2) they possess relative high conversion efficiencies to LCP within the frequency band of interest. The section of method provides more simulation details. Finally, we carefully select 32 different structural parameters containing solid and inverse rectangular structures in Table S1 and present the individual phase responses and conversion efficiencies in Figure S1.To directly present the coversion efficiencies, we provide an efficiency map (as shown in Figure S2) of the selected meta-atoms with respect to different frequencies. Here as an example, Figure 2(c) presents the simulated phase differences of the solid structure (sequence number 15, 580°) and the inverse structure (sequence number 27, 725°) with a same etching depth t = 350 μm, showing the linear phase response as a function of f (or $1/\lambda$). Note that the inverse structures in Table S1 have a wider phase response than the solid structures in Table S1 and can compensate for a larger phase difference, so that the positions of the inverse structures are close to x = 0 and those of the solid structures are close to the left edge of the sample, as shown in Figure 1(a).

Before closing this section, we emphasize that only the LCP component of the transmitted wave can acquire the PB phases under RCP incidence [49, 50], so that only this wave component can generate the desired achromatic Airy beam. Moreover, the metadevice thus constructed does not work for linear-polarization incidence under which the meta-atoms do not generate any PB phase.

2.2 Numerical calculation of THz achromatic Airy beams

To confirm the desired phase profile $\varphi(x,f)$ in Eq. (5) derived by the geometrical construction method and reveal the underlying mechanism of the achromatic Airy beam, we performed numerical calculations based on Fraunhofer diffraction integration. In our numerical results, the structural region ranged along x axis from x = −7 mm to x = +4 mm. Figure 3(a) shows the phase profiles at frequencies f_{min} = 0.4 THz, f = 0.6 THz, and f_{max} = 0.8 THz. Note that the phase profile at 0.8 THz is smaller than that at 0.4 THz, which is in conflict with the relation between transmission phase response and frequency. This impasse is broken by introducing an additional phase shift $\varphi_{shift}(f)$ that is larger than the phase difference $\Delta\varphi$ =

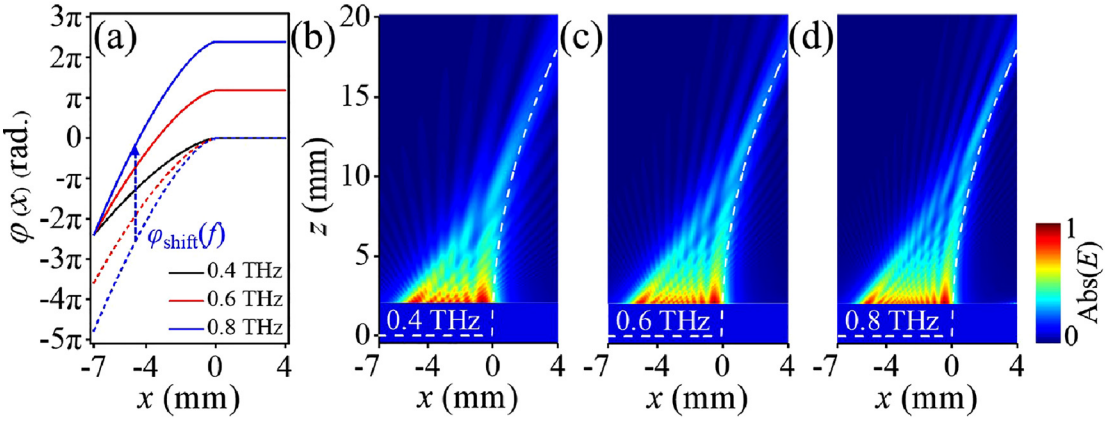

Figure 3: Fraunhofer diffraction integration of the phase profiles in Eq.(2) realized by PB phase.
(a) Phase profile of an achromatic Airy beam with additional phase shift $\varphi_{shift}(f)$. (b), (c) and (d) Numerically calculated Airy beams at frequencies 0.4, 0.6 and 0.8 THz. The white dash lines are the parabolic trajectory curve $f(z)$.

$\varphi_{0.4\mathrm{THz}} - \varphi_{0.8\mathrm{THz}} = 1350^\circ$ at the position $x = -7$ mm. To compensate for the large phase difference, the building structures are no longer subwavelength. In this case, we resort only to the geometric phases of three different angles of rotation with respect to the laboratory coordinate system to match the phase profiles of Airy beams with different frequencies at 0.4, 0.6, and 0.8 THz. Table S2 in the Supplementary material shows the structural parameters and the rotated angle distributions. Subsequently, we performed a numerical calculation based on the initial field $\mathcal{F}\{e^{ik\varphi(x)}\}$, in which all metasurfaces in the array with period 70 μm were considered as subsources radiating cylindrical surface waves with designed initial phase profiles. Figure 3(b–d) shows the numerically calculated Airy beams and Figure S3(a–c) in the Supplementary material show the FDTD simulated beams at frequencies 0.4, 0.6, and 0.8 THz. We find that the trajectories of the Airy beams are in good agreement with the parabolic curve $f(z)$, although they are both imperfect owing to the limited number of metasurface elements and the nonideal phase profiles.

2.3 Experimental setup and fabricated samples

To validate the above theoretical analysis, we designed a silicon metasurface device for generating a broadband THz achromatic Airy beam. However, the theoretical design of achromatic Airy beams requires a phase compensation of 1350°, which can*not* be compensated owing to the large aspect ratio in experimental fabrication. Therefore, we reduced the sample size, which ranges along the x-axis from –3.2 to 4 mm. In our design, we chose the additional phase shift $\varphi_{\mathrm{shift}}(f)$ to be 820° at 0.8 THz. To encode the phase profiles of the achromatic Airy beam within the frequency band, we placed the 32 selected structures at x coordinates with approximately equal phase differences, as shown in Figure S4, in the Supplementary material. The starting points of each vertical line is the initial phase φ_0 at 0.4 THz, and the height of each vertical line is the phase coverage (or phase difference). The unresolved problem is to realize the phase profile at 0.4 THz. Here, the phase profile is taken as the basic phase $\varphi_1(x,f)$, determining the parabolic trajectory of the achromatic Airy beam within the frequency range. The basic phase $\varphi_1(x,f)$ is related solely to f_{min} and is independent of the working frequency f. The PB phase, which is independent of the transmission phase, is used to acquire the phase profile at 0.4 THz. To obtain the correct basic phase $\varphi_1(x, f)$, the spatial rotation angle θ of each structural unit is taken as $\theta = (\varphi_1 - \varphi_0)/2$ (for further details, see Table S3 in the Supplementary material)

To verify the reliability of our designed metasurface devices, we fabricated samples to generate achromatic Airy beams and explore the corresponding characteristics using THz near-field scanning microscopy (NFSM), as shown in Figure 4(a). The polarizer controls the polarization of the light output by the fiber laser, which is focused by the lens and reflected by the mirror, and finally illuminates the light on the probe. In the real system shown in Figure S5 in the Supplementary material, the collimated THz waves radiating from a 100 fs (λ=780 nm) laser-pulse-pumped photoconductive antenna emitter are modulated with an appropriately polarized state. A commercial THz near-field probe is positioned 2 mm away from the sample to detect the E_x of the transmitted LCP light, with the RCP light illuminating the metasurface device. The sample is fabricated on a silicon wafer by conventional lithography together with deep reactive ion etching. Further details of sample fabrication are given in methods. Figure 4(b) shows an optical microscope image of the whole of the fabricated

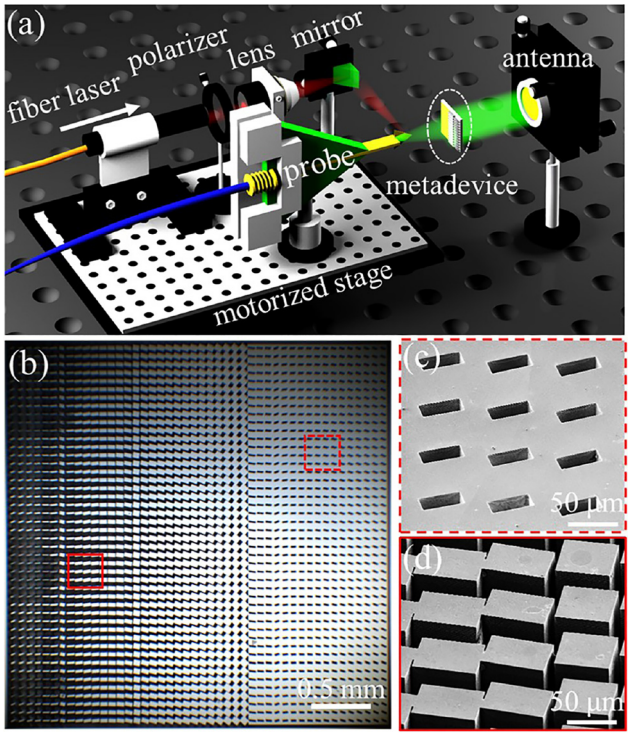

Figure 4: Experimental setup of the terahertz (THz) near-field scanning microscopy (NFSM) and sample images.
(a) Schematic of THz NFSM. (b) Optical image of the whole sample. (c) Partial enlargement on the right side (red desh box) of the inverse structures. (d) Partial enlargement on the left side (red box) of the solid structures.

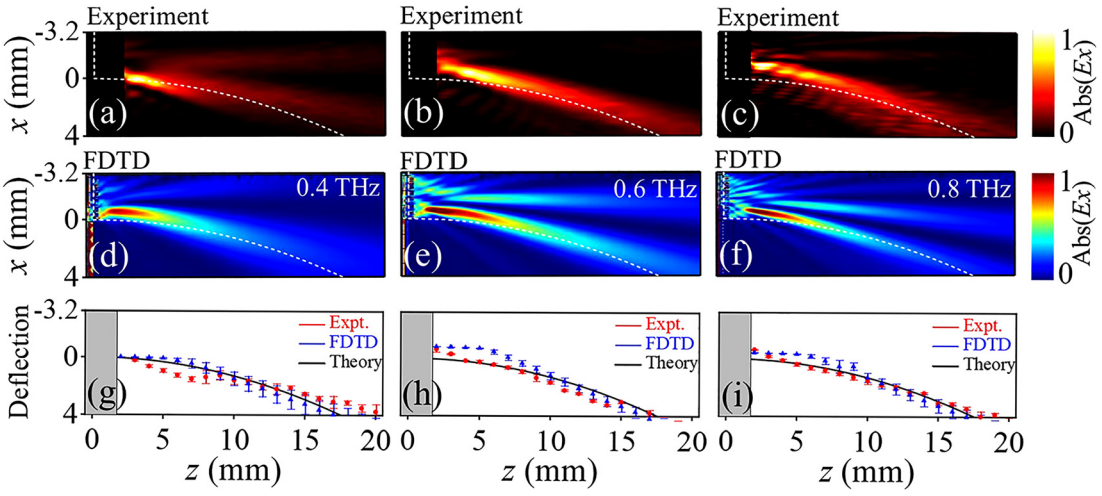

Figure 5: Achromatic Airy beam experiments.
(a)–(c) Experimental results on near-field detections at the three frequencies, showing that the intensity distributions of the left circular polarization (LCP) field transmitted through the metasurface devices match well with the white dash line indicating the parabolic trajectory. (d)–(f) Simulation results at the three frequencies. (g)–(i) Comparison of experiment, simulation, and theoretical deflections, where the error bars correspond to 95% of the maximum normalized intensity.

sample. Figure 4(c) and (d) shows partially enlarged scanning electron microscope (SEM) images of the inverse and solid structures, respectively. Note that the inverse structures with a larger phase compensation are located toward the right of the metasurface device, while the solid structures with a smaller phase compensation are located toward the left side.

2.4 Experimental detection of THz achromatic Airy beams

Figure 5(a)–(c) shows the normalized abs(E_x) distributions of the transmitted LCP light obtained from the THz NFSM at the three frequencies. Note that there are no data for the first 2 mm in the experimental results because of a safety distance imposed during the experiment to prevent collisions. In these figures, the normalized abs(E_x) distributions show a good match with the parabolic trajectory (the white dash line) at 0.4 THz. To verify the experimental results, Figure 5(d)–(f) presents the normalized intensity distributions E_x simulated by FDTD at frequencies 0.4, 0.6, and 0.8 THz, respectively. Furthermore, in Figure S6 in the Supplementary material, we present the results of Fraunhofer diffraction integration at more frequencies, the results of simulation, and experimental data, all of which verify the achromatism of the Airy beams. For a more intuitive comparison between the simulation results and experimental data, we obtain the lateral offsets x of the maximum normalized intensity (with error bars corresponding to 95% of the maximum normalized intensity) at different propagation distances z and compare them with the numerical deflection. Figure 5(g)–(i) shows the results of this comparison at the three frequencies, and it can be seen that there is good agreement. In the simulation, we calculated the working efficiency of the device, as shown in Figure S7 in the Supplementary material. The working efficiency ranges from 20 to 60% and is higher at frequencies near 0.6 THz. Furthermore, we present the simulation results for the self-healing properties of the achromatic Airy beam in the case of scattering by silicon particles in Figure S8 in the Supplementary material.

2.5 THz achromatic Airy-beam-based metalens

Airy-beam-based metalenses have many advantages for detection, such as large depth of focus (DOF) and self-healing properties, and so here we design a metalens based on autofocusing achromatic Airy beams. To realize this, the achromatic Airy-beam-based metalens, a metasurface device composed of two symmetrical structures is designed to generate two counter-propagating achromatic Airy beams. Figure S9 in the Supplementary material shows optical and SEM images of the metasurface device. To highlight the robustness of the Airy-beam-based metalens, an aluminum foil cover is placed over a 1 mm region (ranging along the x-axis from $x = -0.5$ mm to $x = +0.5$ mm) around the center of the experimental sample. Figure 6(d)–(f) shows the normalized abs (E_x) distributions of the metalens at

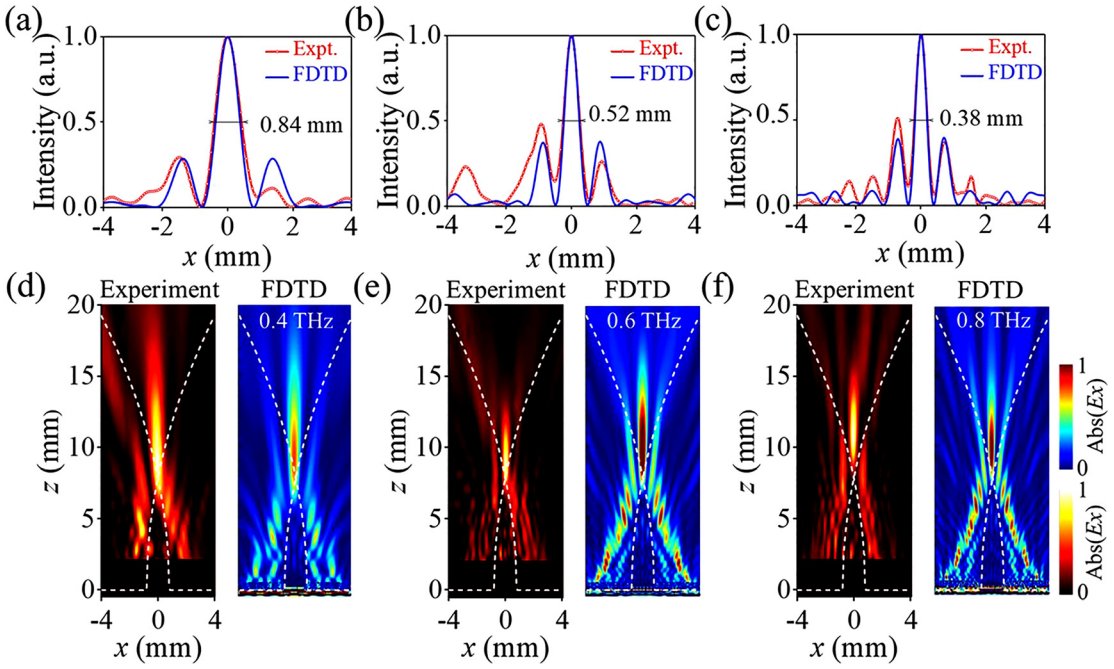

Figure 6: Achromatic Airy beam-based metalens.
(a)–(c) Comparison of simulated and experimental results for the intensity distributions at the focal length. The full width at half maximum (FWHMs) of the intensity distribution are 0.84 mm at 0.4 THz, 0.52 mm at 0.6 THz, and 0.38 mm at 0.8 THz. (d)–(f) Demonstration of the generation of two counter-propagating achromatic Airy beams in experiments and simulations. The focal length $f = 10$ mm.

frequencies 0.4, 0.6 and 0.8 THz, respectively. Experimental results are presented on the left and FDTD results on the right. Experimental results at other frequencies are shown in Figure S10 in the Supplementary material. In particular, it should be noted that there is less energy in the region covered by aluminum foil, which is quite different from what occurs with a traditional metalens. The intensity distributions in the vertical direction at the center of the two cases can be found in Figure S11 in the Supplementary material. A comparison shows that the Airy-beam-based metalens has the advantage of a larger DOF and detection with a high signal-to-noise ratio. Interestingly, the starting points of the autofocusing effect fit well with the intersection of the parabolic trajectory. When two counter-propagating achromatic Airy beams begin to intersect, constructive interference occurs, and the trajectory curves coincide with the lower edge of the normalized intensity distributions of the focal spots. Furthermore, because the full width at half maximum (FWHM) of the focal spots is the main indicator to evaluate the performance of Airy-beam-based metalenses, we compared the experimental and theoretical distributions at a focal length $f = 10$ mm and measured the FWHM at the three frequencies, as shown in Figure 6(a)–(c). The FWHM is 0.84 mm at 0.4 THz ($\lambda = 0.75$ mm), 0.52 mm at 0.6 THz ($\lambda = 0.5$ mm), and 0.38 mm at 0.8 THz ($\lambda = 0.375$ mm). The experimental results agree well with those of the simulations, and the FWHMs are approximately equal to the wavelength of incidence of the THz wave. The self-healing property is typically verified by placing an obstacle on the travel path of the parabolic trajectory. The trajectory recovers quickly if two silicon obstacles of diameter 400 μm are located at (x, z) = (–0.8 mm, 6 mm) and (0.8 mm, 6 mm), indicating a rather robust self-healing property of the generated Airy-beam-based metalens. The self-bending, diffraction-free, and self-healing achromatic properties are illustrated in Figure S12 in the Supplementary material.

3 Conclusion

We have experimentally demonstrated achromatic Airy beams in the THz regime using carefully designed silicon metasurface devices. Furthermore, we have shown numerically that a metalens based on an achromatic Airy beam has the advantages of a larger DOF and a self-healing property compared with a traditional achromatic metalens. The achromatic Airy beam developed in this paper has important potential applications to light-sheet microscopy, self-healing metalens bio-imaging, and high signal-to-noise ratio detection.

4 Methods

4.1 Simulation details

FDTD was used to find and simulate the structural units and the transmission E_x field of the metasurface devices. In the simulation of the unit, the mesh grid size was set to 10 nm. In the simulation of the whole metasurface device, the grid size was set to 1 μm

4.2 Sample fabrication

All the silicon metasurface devices were fabricated using conventional lithography together with deep reactive ion etching. The refractive index n of silicon is 3.45 and its resistance R is higher than 10^4 Ω cm. First, a 2-μm-thick silica layer was grown on a 500-μm-thick double-side-polished high-resistivity silicon wafer. Next, by conventional photolithography, the left photoresist and the silica became a double layer of protection above the silicon posts. Conventional deep reactive ion etching was then employed to make silicon posts of thickness t = 350 μm. Finally, the remaining photoresist and the remaining silica were cleaned off separately.

4.3 Experimental characterization

THz near-field scanning microscopy was employed in the experimental tests owing to its high scanning speed and high resolution. Here, only the x-polarized electric field E_x component was measured with RCP illumination. The electric field was detected at 0.2 mm intervals from −3.2 to 4 mm in both the x and z directions. Note that we reserved 2 mm to avoid collisions between the probe and the metasurface devices.

Author contributions: Q.C., J.W. and L.M. contributed equally to this work. J.C., L.M., Z.S., J.Z., and X.Z. carried out simulations, fabricated the samples and conducted part of the measurements; J.W., T.C., Y.Y., and D.Y. did the theoretical calculations and designed the samples; J.W. and Z.S. built the experimental setup and conducted part of measurements; Q.H. and W.H. provided technical supports for simulations and data analyses. Q.C., S.Z. and L.Z. organized the project, designed experiments and analyzed the results. All the authors contributed to the preparation of the manuscript, and have accepted responsibility for the entire content of this submitted manuscript and approved submission.

Research funding: This work was funded by National Natural Science Foundation of China (No. 11874266, No. 11604208, No. 11734007, No. 91850101, No. 11674068, No. 11874118), National Key Research and Development Program of China (No. 2017YFA0303504 and No. 2017YFA0700201), Chenguang Program (17CG49), Natural Science Foundation of Shanghai (No.20JC1414601 and No.18ZR1403400).

Conflict of interest statement: The authors declare no conflicts of interest regarding this article.

References

[1] M. V. Berry and N. L. Balazs, "Nonspreading wave packets. Nonspreading wave packets," *Am. J. Phys.*, vol. 47, p. 264, 1979.
[2] M. Henstridge, C. Pfeiffer, D. Wang, et al., "Accelerating light with metasurfaces," *Optica*, vol. 5, p. 678, 2018.
[3] G. A. Siviloglou, J. Broky, A. Dogariu, and D. N. Christodoulides, "Observation of accelerating airy beams," *Phys. Rev. Lett.*, vol. 99, p. 213901, 2007.
[4] Y. Lumer, Y. Liang, R. Schley, et al., "Incoherent self-accelerating beams," *Optica*, vol. 2, p. 886, 2015.
[5] A. Salandrino and D. N. Christodoulides, "Airy plasmon: a nondiffracting surface wave," *Opt. Lett.*, vol. 35, p. 2082, 2010.
[6] J. Broky, G. A. Siviloglou, A. Dogariu, and D. N. Christodoulides, "Self-healing properties of optical airy beams," *Opt. Express*, vol. 16, p. 12880, 2008.
[7] N. K. Efremidis, Z. Chen, M. Segev, and D. N. Christodoulides, "Airy beams and accelerating waves: An overview of recent advances," *Optica*, vol. 6, p. 686, 2019.
[8] J. Baumgartl, M. Mazilu, and K. Dholakia, "Optically mediated particle clearing using airy wavepackets," *Nat. Photonics*, vol. 2, p. 675, 2008.
[9] A. Chong, W. H. Renninger, and D. N. Christodoulides, "Airy–bessel wave packets as versatile linear light bullets," *Nat. Photonics*, vol. 4, p. 103, 2010.
[10] D. Abdollahpour, S. Suntsov, D. G. Papazoglou, and S. Tzortzakis, "Spatiotemporal airy light bullets in the linear and nonlinear regimes," *Phys. Rev. Lett.*, vol. 105, p. 253901, 2010.
[11] S. Jia, J. C. Vaughan, and X. Zhuang, "Isotropic three-dimensional super-resolution imaging with a self-bending point spread function," *Nat. Photonics*, vol. 8, p. 302, 2014.
[12] S. Jia, "Super-resolution imaging with airy beams," in *Laser Sci*, vol. 180, p. 2520, 2015.
[13] Q. Fan, D. Wang, P. Huo, Z. Zhang, Y. Liang, and T. Xu, "Autofocusing airy beams generated by all-dielectric metasurface for visible light," *Opt. Express*, vol. 25, p. 9285, 2017.
[14] P. Zhang, J. Prakash, Z. Zhang, et al., "Trapping and guiding microparticles with morphing autofocusing airy beams," *Opt. Lett.*, vol. 36, p. 2883, 2011.
[15] M. Manousidaki, D. G. Papazoglou, M. Farsari, and S. Tzortzakis, "Abruptly autofocusing beams enable advanced multiscale photo-polymerization," *Optica*, vol. 3, p. 525, 2016.
[16] T. Vettenburg, H. I. Dalgarno, J. Nylk, et al., "Light-sheet microscopy using an airy beam," *Nat. Methods*, vol. 11, p. 541, 2014.
[17] G. A. Siviloglou and D. N. Christodoulides, "Accelerating finite energy airy beams," *Opt. Lett.*, vol. 32, p. 979, 2007.
[18] T. Latychevskaia, D. Schachtler, and H.-W. Fink, "Creating airy beams employing a transmissive spatial light modulator," *Appl. Opt.*, vol. 55, p. 6095, 2016.
[19] P. Zhang, S. Wang, Y. Liu, et al., "Plasmonic airy beams with dynamically controlled trajectories," *Opt. Lett.*, vol. 36, p. 3191, 2011.
[20] B.-Y. Wei, P. Chen, S.-J. Ge, W. Duan, W. Hu, and Y.-Q. Lu, "Generation of self-healing and transverse accelerating optical vortices," *Appl. Phys. Lett.*, vol. 109, p. 121105, 2016.
[21] A. Minovich, A. E. Klein, N. Janunts, T. Pertsch, D. Neshev, and Y. S. Kivshar, "Generation and near-field imaging of airy surface plasmons," *Phys. Rev. Lett.*, vol. 107, p. 116802, 2011.

[22] L. Li, T. Li, S. Wang, C. Zhang, and S. Zhu, "Plasmonic airy beam generated by in-plane diffraction," *Phys. Rev. Lett.*, vol. 107, p. 126804, 2011.
[23] F. Aieta, P. Geneve, N. Yu, M. A. Kats, Z. Gaburro, and F. Capasso, "Out-of-plane reflection and refraction of light by anisotropic optical antenna metasurfaces with phase discontinuities," *Nano Lett.*, vol. 12, p. 1702, 2012.
[24] A. Pors and S. I. Bozhevolnyi, "Plasmonic metasurfaces for efficient phase control in reflection," *Opt. Express*, vol. 21, p. 27438, 2013.
[25] Z. Li, E. Palacios, S. Butun, and K. Aydin, "Visible-frequency metasurfaces for broadband anomalous reflection and high-efficiency spectrum splitting," *Nano Lett.*, vol. 15, p. 1615, 2015.
[26] C. Pfeiffer and A. Grbic, "Controlling vector bessel beams with metasurfaces," *Phys. Rev. Appl.*, vol. 2, p. 044012, 2014.
[27] A. Arbabi, Y. Horie, M. Bagheri, and A. Faraon, "Dielectric metasurfaces for complete control of phase and polarization with subwavelength spatial resolution and high transmission," *Nat. Nanotechnol.*, vol. 10, p. 937, 2015.
[28] Z. Wang, S. Dong, W. Luo, et al., "High-efficiency generation of bessel beams with transmissive metasurfaces," *Appl. Phys. Lett.*, vol. 112, p. 191901, 2018.
[29] A. Shaltout, J. Liu, A. Kildishev, and V. Shalaev, "Photonic spin hall effect in gap–plasmon metasurfaces for on-chip chiroptical spectroscopy," *Optica*, vol. 2, p. 860, 2015.
[30] S. Sun, Q. He, J. Hao, and L. Zhou, "Electromagnetic metasurfaces: physics and applications," *Adv. Opt. Photonics*, vol. 11, p. 380, 2019.
[31] X. Luo, "Subwavelength optical engineering with metasurface waves," *Adv. Opt. Mater.*, vol. 6, p. 1701201, 2018.
[32] V. C. Su, C. H. Chu, G. Sun, and D. P. Tsai, "Advances in optical metasurfaces: fabrication and applications," *Opt. Express*, vol. 26, p. 13148, 2018.
[33] S. M. Kamali, E. Arbabi, A. Arbabi, and A. Faraon, "A review of dielectric optical metasurfaces for wavefront control," *Nanophotonics*, vol. 7, p. 1041, 2018.
[34] W. T. Chen, A. Y. Zhu, and F. Capasso, "Flat optics with dispersion-engineered metasurfaces," *Nat. Rev. Mater.*, pp. 1–17, 2020. https://doi.org/10.1038/s41578-020-0203-3.
[35] M. Jia, Z. Wang, H. Li, et al., "Efficient manipulations of circularly polarized terahertz waves with transmissive metasurfaces," *Light Sci. Appl.*, vol. 8, pp. 1–9, 2019.
[36] Q. Yang, X. Chen, Q. Xu, et al., "Broadband terahertz rotator with an all-dielectric metasurface," *Photonics Res.*, vol. 6, p. 1056, 2018.
[37] Q. Wang, Q. Xu, X. Zhang, et al., "All-dielectric meta-holograms with holographic images transforming longitudinally," *ACS Photonics*, vol. 5, p. 599, 2018.
[38] Z. Li, H. Cheng, Z. Liu, S. Chen, and J. Tian, "Plasmonic airy beam generation by both phase and amplitude modulation with metasurfaces," *Adv. Opt. Mater.*, vol. 4, p. 1230, 2016.
[39] H. Wang, J. Du, H. Wang, Y. Lu, and P. Wang, "Generation of spin-dependent accelerating beam with geometric metasurface," *Adv. Opt. Mater.*, vol. 7, 2019, https://doi.org/10.1002/adom.201900552.
[40] H. Li, W. Hao, X. Yin, S. Chen, and L. Chen, "Broadband generation of airy beams with hyperbolic metamaterials," *Adv. Opt. Mater.*, p. 1900493, 2019, https://doi.org/10.1002/adom.201900493.
[41] E. Y. Song, G. Y. Lee, H. Park, et al., "Compact generation of airy beams with c-aperture metasurface," *Adv. Opt. Mater.*, vol. 5, p. 1601028, 2017.
[42] W.-L. Guo, K. Chen, G.-M. Wang, et al., "Airy beam generation: approaching ideal efficiency and ultra wideband with reflective and transmissive metasurfaces," *Adv. Opt. Mater.*, vol. 8, p. 2000860, 2020.
[43] E. Arbabi, A. Arbabi, S. M. Kamali, Y. Horie, and A. Faraon, "Controlling the sign of chromatic dispersion in diffractive optics with dielectric metasurfaces," *Optica*, vol. 3, p. 628, 2016.
[44] S. Wang, P. C. Wu, V.-C. Su, et al., "Broadband achromatic optical metasurface devices," *Nat. Commun.*, vol. 8, p. 187, 2017.
[45] M. Khorasaninejad, F. Aieta, P. Kanhaiya, et al., "Achromatic metasurface lens at telecommunication wavelengths," *Nano Lett.*, vol. 15, p. 5358, 2015.
[46] S. Wang, P. C. Wu, V.-C. Su, et al., "A broadband achromatic metalens in the visible," *Nat. Nanotechnol.*, vol. 13, p. 227, 2018.
[47] Q. Cheng, M. Ma, D. Yu, et al., "Broadband achromatic metalens in terahertz regime," *Sci. Bull.*, vol. 64, p. 1525, 2019.
[48] W. T. Chen, A. Y. Zhu, V. Sanjeev, et al., "A broadband achromatic metalens for focusing and imaging in the visible," *Nat. Nanotechnol.*, vol. 13, p. 220, 2018.
[49] W. Luo, S. Sun, H.-X. Xu, Q. He, and L. Zhou, "Transmissive ultrathin pancharatnam-berry metasurfaces with nearly 100," *Phys. Rev. Applied*, vol. 7, p. 044033, 2017.
[50] W. Luo, S. Xiao, Q. He, S. Sun, and L. Zhou, "Photonic spin hall effect with nearly 100% efficiency," *Adv. Opt. Mater.*, vol. 3, no. 8, pp. 1102–1108, 2015.

Supplementary Material: The online version of this article offers supplementary material (https://doi.org/10.1515/nanoph-2020-0536).